IOP Concise Physics

Basic Surfaces and their Analysis

Lyudmila V Goncharova

Chapter 7

Ion scattering and high-resolution ion depth profiling methods

In this section, the fundamentals of ion beam methods are presented along with a summary of the limitations and capabilities specific for each method. We start with classical concepts of atomic collisions as applied to Rutherford scattering, review energy losses and electron interactions, and examine how they are applicable to Rutherford backscattering spectroscopy. An overview of experimental methods with incident ion beams, such as secondary ion mass spectroscopy, low- and medium-energy scattering, will be provided at the end of this chapter.

7.1 Ion–solid interactions

First, let us consider a broader variety of processes that may happen when energetic ions interact with the surface and near-surface layers of the material, as illustrated in figure 7.1. In Rutherford backscattering spectrometry (RBS), monoenergetic light incident ions collide with target atoms and are scattered in all possible directions. Backscattered ions will be analyzed in the detector by measuring the energies of the ions. In elastic collisions not all the particles are scattered in the backward direction, especially when the mass of the incident ion is equal to or greater than that of the target atom. In this case, the energy of the incident beam is transferred to lighter target atoms in a recoil process, being used in elastic recoil detection analysis (ERDA). Additionally, while traveling through the material, MeV ions can produce inner shell ionization, characteristic x-rays will be emitted and these x-rays will be detected in proton (particle) induced x-ray emission (PIXE). In nuclear reaction analysis (NRA), incident ion particles of a particular energy can excite the target nucleus to a higher energy state; the nucleus can then de-excite by γ-rays' emission. Finally, surface layers are eroded by a sputtering process with keV incident ions. The abundant sputtered species, ions and ion clusters, are accelerated and they provide a direct measure of the composition of the surface layers in secondary ion mass

doi:10.1088/978-1-6817-4954-9ch7

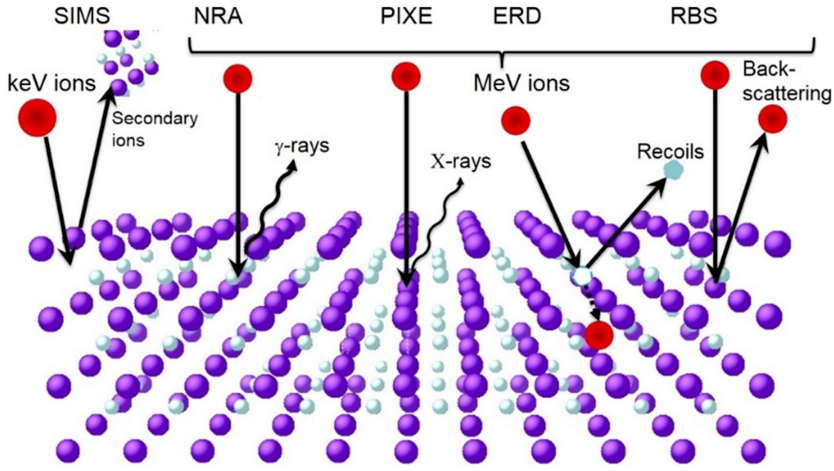

Figure 7.1. Diagram of possible scattering and excitation events during ion–solid interactions.

spectroscopy, SIMS. More detailed discussions of ion–solid interactions can be found in several textbooks [1, 2].

In RBS, energy is transferred from the moving particle to the stationary target atom; the reduction in energy of the scattered particle depends on the masses of incident and target atoms and provides the signature of the target atoms. The equation concerning the energy transfer or kinematics inelastic collisions between two isolated particles can be solved fully by applying the conservation of energy and momentum in two dimensions, as shown on the diagram below (figure 7.2).

An incident energetic particle of mass M_1 has velocity v_0 and energy E_0, and the target atom of mass M_2 is at rest. After the collision, the values of the velocities v_1 and v_2, the projectile and target atom trajectories are determined by the scattering angle, θ, and recoil angle, ϕ as presented in figure 7.2. Conservation of energy and conservation of momentum parallel and perpendicular to the direction of incidence can be expressed by the following equations:

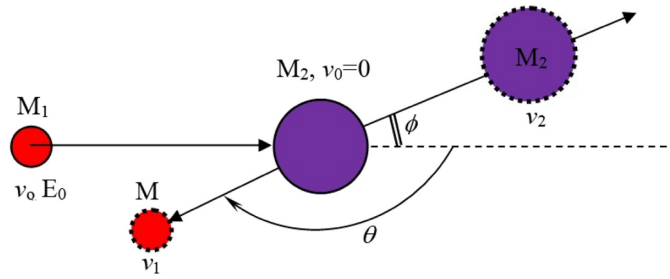

Figure 7.2. Diagram of the elastic collision between the projectile of mass M_1, velocity v_o and energy E_o and a target mass M_2, initially at rest. After the collision, the projectile and the target mass have velocities and energies v_1, E_1 and v_2, E_2.

$$\frac{1}{2}M_1v^2 = \frac{1}{2}M_1v_1^2 + \frac{1}{2}M_2v_2^2 \tag{7.1}$$

$$M_1v = M_1v_1\cos\theta + M_2v_2\cos\phi \tag{7.2}$$

$$0 = M_1v_1\sin\theta - M_2v_2\sin\phi \tag{7.3}$$

By solving these equations, eliminating ϕ, then v_2, we can find the ratio of the ion velocities:

$$\frac{v_1}{v_0} = \frac{[\pm(M_2^2 - M_1^2\sin^2\theta)^{1/2} + M_1\cos\theta]}{M_1 + M_2} \tag{7.4}$$

If $M_1 < M_2$, the plus sign holds and the ratio of the projectile energies is

$$k = \frac{E_1}{E_o} = \left[\frac{(M_2^2 - M_1^2\sin^2\theta)^{1/2} + M_1\cos\theta}{M_2 + M_1}\right]^2 \tag{7.5}$$

The energy ratio is also called the kinematic factor, k, and it shows that energy after collision is determined by the masses of the particle and target atom and scattering angle, θ. A plot of the calculated kinematic factor, k, versus scattering angle for protons (H^+) and scattering from various target atoms is shown in figure 7.3. A larger separation between the dispersion curves is achieved at larger scattering angles (approaching 180 degrees); this is why the backward geometries (detectors at θ = 150–170 degrees) are typically used in most common RBS experiments. Note that the dispersion curves will separate better if He ions or heavier projectiles are utilized as incident particles.

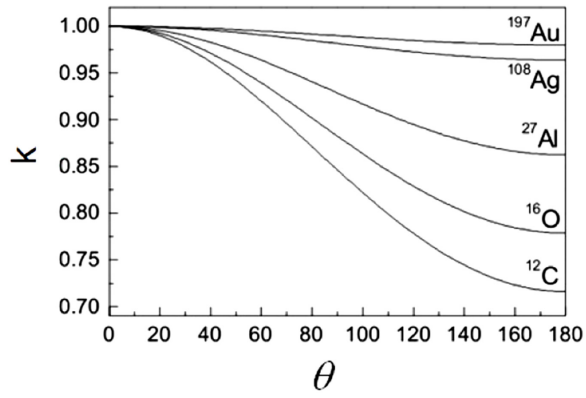

Figure 7.3. Dispersion relationship of the kinematic factor, k, for scattering angle θ for different target masses (C, O, Al, Ag and Au).

Furthermore, in collisions where masses M_1 and M_2 are comparable or equal, the incident particles will be at rest after the collision with all the energy transferred to the target atom. For $\theta = 180°$, the energy E_2 transferred to the target atom has its maximum value at

$$\frac{E_2}{E_0} = \frac{4M_1M_2}{(M_1 + M_2)^2} \tag{7.6}$$

A more general relationship given by equation (7.7) will be used later in the section dedicated to elastic recoil detection analysis:

$$\frac{E_2}{E_0} = \frac{4M_1M_2}{(M_1 + M_2)^2}\cos^2\phi \tag{7.7}$$

It is important to note here that scattering will be determined by a central force provided by the Coulomb force F at a distance R. As the particle with charge Z_1e approaches the target atom, charge Z_2e, it will experience a repulsive force that will cause its trajectory to deviate from the straight line. The value of the Coulomb force is $F = \frac{Z_1Z_2e^2}{r^2}$.

In addition to easy analytical expressions (equation (7.5)) that can be used to identify masses within the material, scattering cross-sections are very well known in the energy range 0.5–4.0 MeV. Incident MeV ions do not only scatter from the atoms on the surface, they also penetrate fairly deeply inside the solid. Therefore, we can get information about buried interfaces and single crystal substrates. Single crystals are not rare in modern day technology as many nanoelectronic components are based on single-crystal semiconductors.

The influence of the crystal lattice field on the trajectories of ions traveling deeper into material is known as *channeling*. When incident ions interact with amorphous or disordered materials, as presented schematically in figure 7.4(a), almost none of

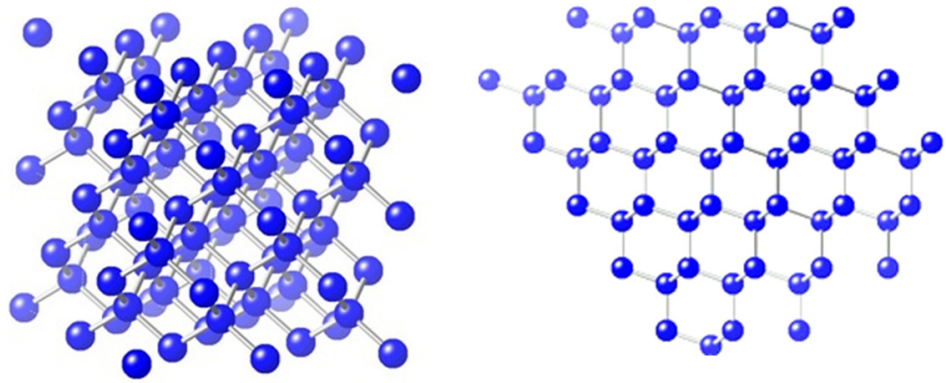

Figure 7.4. Schematic diagram showing the arrangement of Si atoms in (a) an amorphous and (b) single-crystal silicon sample.

the atoms deeper in the solid are obstructed by surface atoms. In other words, all atoms are visible to incident ions and collisions can take place. Channeling of energetic ions occurs when the incident beam is carefully aligned with one of the major crystallographic directions in a crystal (figure 7.4(b)). In this direction, ions travel between rows or planes of atoms. If channeled ions cannot get close enough to the atomic nuclei, they will undergo large angle scattering. This effect reduces the scattering yield from the single crystal substrate by a factor of 10–50. However, atoms in the surface layer, disordered regions, dopant atoms and amorphous regions will be visible to the ion beam.

In the channeling geometry, the ion yield is greatly reduced if the subsurface atoms are in their ideal lattice positions. However, atoms in the disordered and amorphous regions will be visible to the ion beam. Thus, the degree of crystallinity of the samples can be determined by taking the ratio of the yield in the channeling geometry to a random direction yield ('the maximum yield').

7.2 Stopping and range of ions in matter (SRIM)

The penetration of ions in matter was a subject of great interest in the 1950s. The energy of particles could be determined by measurements of their absorption by various materials. The number of detected particles stayed practically constant with increased separation between the ion source and the detector up to a distance R, and then dropped to zero. The distance R is the range of the particles and it can be defined by

$$R = \int_0^{E0} \left(\frac{\mathrm{d}E}{\mathrm{d}x}\right)^{-1} \mathrm{d}E \tag{7.8}$$

where E_o is the initial kinetic energy and $\mathrm{d}E/\mathrm{d}x$ is the energy lost per unit path length, $\mathrm{d}x$.

In 1963, the first unified approach to stopping and range theory was proposed by Lindhard, Scharff and Schiott [3], an approach commonly called the LSS theory. The LSS theory was the last of the comprehensive theories based on statistical models of atom–atom collisions. Improvements in calculating stopping and ranges over the next 20 years were made by using numerical techniques and removing some of the approximations used by Bohr, Firsov and Lindhard. Stopping powers can now be calculated with an average accuracy of about 5% overall, 6% for heavy ions and better than 2% for high velocity light ions. Range distributions for amorphous elemental targets have about the same accuracy [4]. A powerful Monte-Carlo code, Stopping and Range of Ions in Matter (SRIM), was developed by Ziegler, Biersack and Ziegler. It allows one to calculate the stopping and range of ions (10 eV–2 GeV amu^{-1}) into matter using a quantum mechanical treatment of ion–atom collisions. During collisions, the ion and atom have a screened Coulomb collision, including exchange and correlation interactions between the overlapping electron shells. The ion also has long range interactions with target atoms creating electron excitations and plasmons within the target. These are described by including a description of the target's collective electronic structure and interatomic bond structure when the calculation is set up. Some examples of the simulations using the

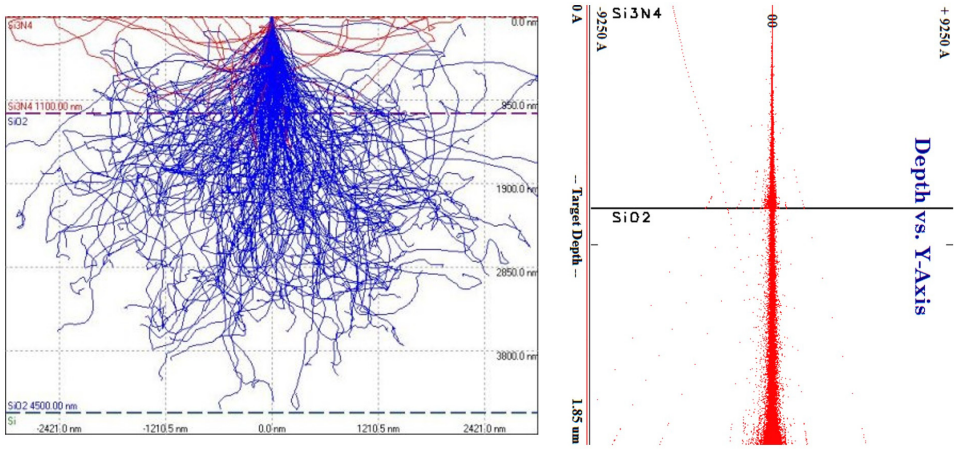

(a) (b)

Figure 7.5. Screenshot from simulation codes illustrating a beam of electrons (a) and ions (b) interacting with silicon nitride/SiO_2 samples.

SRIM code will be provided in the following sections to illustrate the details pertaining to ion–solid interactions.

Another notable detail: when an ion collides with electron clouds in the solid, it does not lose much energy and its direction of motion hardly changes, in contrast to electrons colliding with electrons (figure 7.5).

7.3 Sputtering

Sputtering is the erosion of samples by bombardment of energetic ions or ionic clusters. In this process surface atoms are removed by collisions between the incident particles and the atoms or molecules in the near-surface layer of the material. Sputtering is a very important tool for compositional depth profiling with surface analysis techniques, such as XPS, AES or SIMS. The sputtering process involves a complex series of collisions (the collision cascade) with a sequence of energy transfer between atoms and angular deflections. The simulations are typically based on transport theory that takes into account the dynamics of collision cascade and calculates the energy flux in forward and backward directions. One of the most important parameters in such simulations is the energy deposited at the surface.

The surface of the material erodes under ion bombardment. The sputtering or erosion rates are characterized by the sputtering yield, *Y,* which is defined as the mean number of sputtered target atoms per incident ion:

$$Y = \frac{\text{atoms removed}}{\text{incident ion}} \tag{7.9}$$

Sputtering yield depends strongly on the incident ion energy, mass and scattering geometry, as well as the structure and composition of the target material. Measured

values of Y are in the range $10^{-5} \leqslant Y \leqslant 10^{3}$. The sputtering yields of light ions with MeV energy used in RBS are of the order of 10^{-3}. While for the medium mass ion species and keV energies, $0.5 \leqslant Y \leqslant 20$.

In the linear cascade regime, the number of recoils is proportional to the energy deposited per unit depth. The sputtering yield for particles normal to the surface is

$$Y = \Lambda F_D(E_o) \tag{7.10}$$

where Λ is a constant dependent on the material's binding energy, and $F_D(E_o)$ is the density of deposited energy at the surface. $F_D(E_o)$ depends on the type, energy and direction of the incident ion and target characteristics, such as atomic density and the nuclear cross-section.

Sputtering yields can be relatively accurately predicted by the theory for single-element materials. A TRIM program can be used to a first approximation to estimate the sputtering yields for different scattering angles (figure 7.6(a)) and incident energies (figure 7.6(c)) for amorphous Si. For any given ion-target combination, it is also possible to refer to the published values of the sputtering yields coming from experimental measurements. There are a number of review articles and books that are listed in the references at the end of this chapter [5–8].

When incident ions interact with a multicomponent system, the influence of preferential sputtering and surface segregation must be considered. For a homogeneous material with two components, A and B (let us assume that B has a smaller mass than A), their initial distribution on the surface and in the bulk will be different from the distribution measured after sputtering. Atom B will be displaced and sputtered more than A. This may significantly influence the elemental depth profiles measured with the assistance of sputtering. Material component B will be preferentially removed from the system. For instance, metal oxides will be always slightly reduced since oxygen is preferentially sputtered compared to metal.

In applications when systems with multiple layers are analyzed, penetration of ions can also induce intermixing between one layer and another within the collision

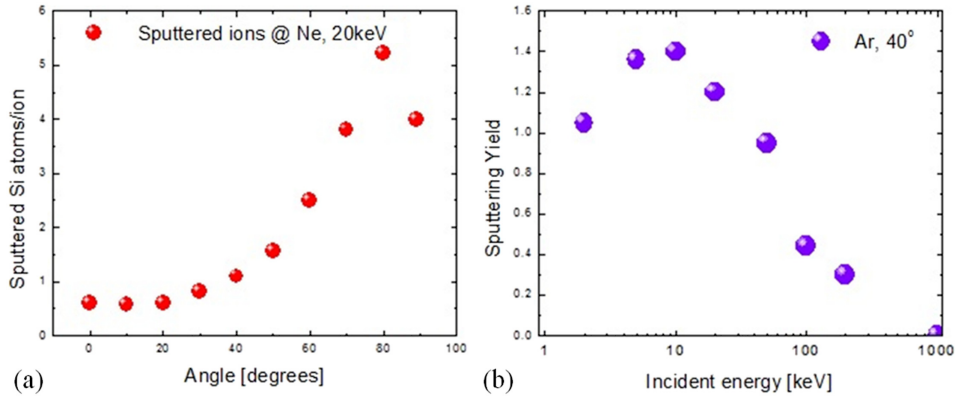

Figure 7.6. (a) Energy dependence of the Ne (20 keV) sputtering yield of Si and (b) incident ion energy dependence of the amorphous Si, calculated by TRIM 2013.

cascade around the ion track. The intermixing leads to an artificial broadening of the concentration depth profiles at the interface. An example of intermixing and interface broadening for 20 Å SiO_2/50 Å Si/5 Å Ta/10 μm C multiple layer stack is shown in figure 7.7.

To summarize, multiple factors may affect elemental depth profiling when sputtering is used. Due to ion bombardment, atomic mixing will change the original compositions, sputtering will induce additional surface roughness, and preferential sputtering will cause compounds to decompose and the composition will be different. Finally, enhanced diffusion and segregation at the surfaces and interfaces are common.

7.4 Rutherford backscattering spectrometry and elastic recoil detection

In Rutherford backscattering spectrometry, monoenergetic ions, typically 500 keV–4 MeV H^+ or He^+, collide with target atoms and a small fraction of incident ions

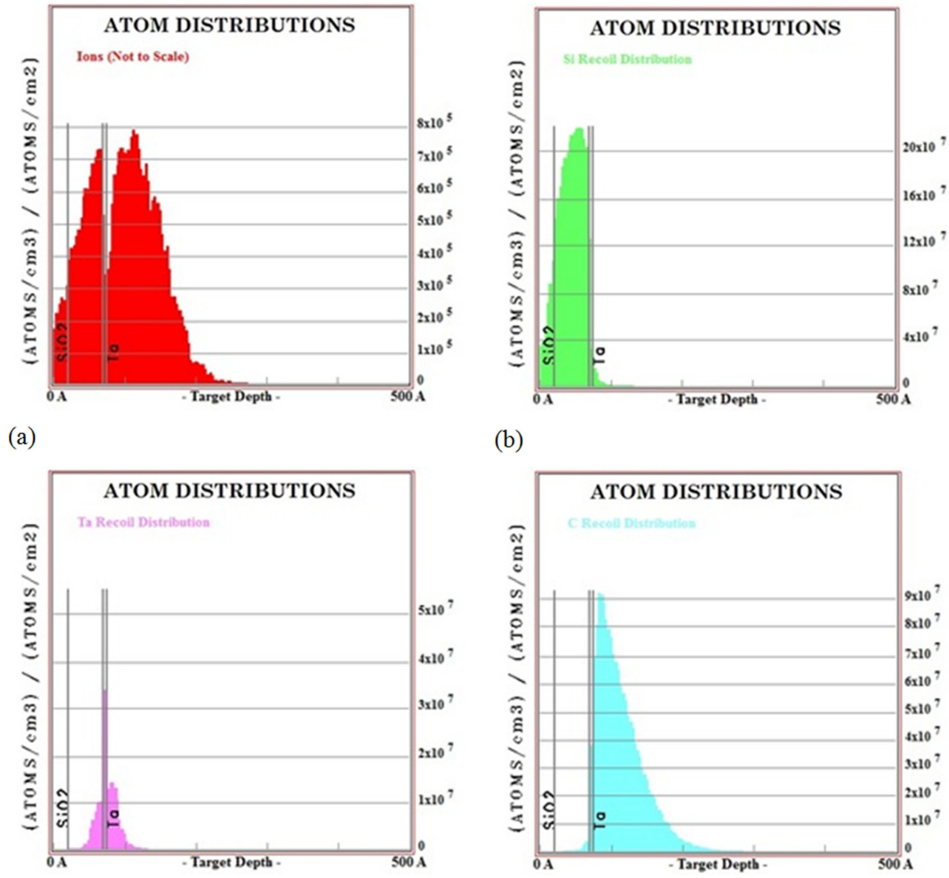

Figure 7.7. Preferential sputtering for a target composing of 20 Å SiO_2/50 Å Si/5 Å Ta/10 μm C with Ar at 10 keV, 45° (a) Ar, (b) Si recoil, (c) Ta recoil and C recoil distribution calculated by TRIM 2013.

scatters back into the detector. In the collision processes discussed previously in section 7.1, the energy is transferred from the moving ion to the stationary target atom. The change in the energy of the scattered particle depends on the masses of the incident and target atoms and the scattering angle (equation (7.4)), and thus provides information of the composition on the surface.

Figure 7.8 shows a backscattering spectrum from a sample with just a few monolayers of C, O, Fe, Mo, Au, 3×10^{16} atoms/cm^2, each on amorphous Si substrate. Various elements' peaks are well separated and can be quantified. The intensity of the peaks, or scattering yields, are strongly dependent on the atomic number of the element. Quantification of atomic densities can be done, since Rutherford scattering cross-sections, σ, are known with high precision and can be estimated by

$$\frac{d\sigma}{d\Omega} \equiv \sigma(\theta) = \left(\frac{Z_1 Z_2 e^2}{4E \sin^2\left(\frac{\theta}{2}\right)} \right)^2 \tag{7.11}$$

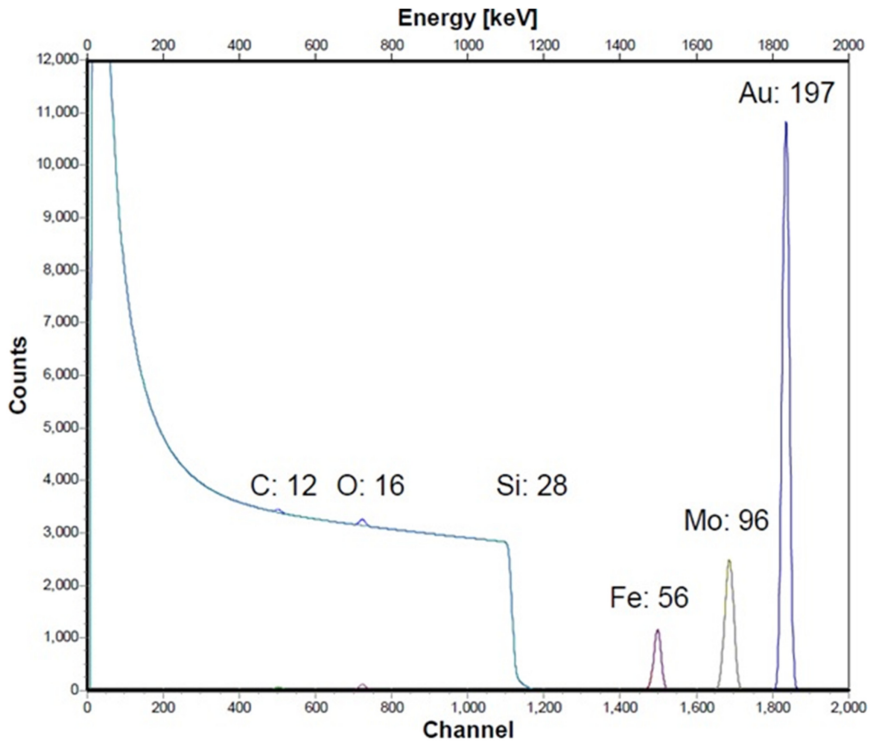

Figure 7.8. Backscattering spectrum (2 MeV $^4He^+$, $\theta = 165°$) from the target containing Au, Mo, Fe, O and C in the surface layer.

where Z_1, and Z_2 are the atomic numbers of the incident ions and target atoms, E is energy during collision and θ is scattering angle. Note that RBS sensitivity will increase with increasing Z_1, increasing Z_2 and decreasing E. This is the scattering cross-section originally derived by Rutherford and is often referred to as a 'Rutherford cross-section'.

The integrated peak intensity A_i for each element on the surface can be calculated using equation (7.12),

$$A_i = (Nt)_i \times Q \times \Omega \times (\sigma(E, \theta)/\cos\theta) \tag{7.12}$$

where $(Nt)_i$ is the areal density or atoms per unit area; Q is the ion beam dose or fluency; Ω is the solid angle of the detector, and $(\sigma(E, \theta)/\cos\theta)$ is the cross-section of the element. Ion dose (fluency), the number of incident particles (collected charge), is measured by a Faraday cup and calculated as $Q = I \times t$. The solid angle, typically in steradians, stays constant for particular detector and slit combinations, and in practice needs to be verified by calibration standard measurements.

An energetic ion that hits a target will not only scatter from the surface atoms but also will penetrate into the target. The energy loss process is described by the stopping cross-section ε defined by

$$\varepsilon(E_o) = \frac{1}{N}\lim_{\Delta x \to 0}\frac{\Delta E}{\Delta x} = \frac{1}{N}\frac{\mathrm{d}E}{\mathrm{d}x}(E_o) \tag{7.13}$$

If the stopping cross-section for a given target is known, then one can find the energy of an ion at any distance x along the ion path:

$$E(x) = E_o - N\int_0^x \varepsilon\,\mathrm{d}x \tag{7.14}$$

And the same is true in the opposite direction. If the energy $E(x)$ of the scattered ion is known, the depth, x, can be calculated:

$$x = \frac{1}{N}\int_{E(x)}^{E0}\frac{1}{\varepsilon}\,\mathrm{d}E\;\mathrm{d}x \tag{7.15}$$

As follows from equation (7.15), the energy of the ion in the backscattering experiment depends on the depth at which scattering from the target atom has occurred. By performing a simulation, the depth profile of the target atoms can be extracted from the measured scattered ion energy distribution.

As the ion passes through the target, it loses energy. The radii of atomic nuclei are so small compared to atomic dimensions that nuclear scattering is rare compared to interactions with electrons. So, in the first approximation, nuclear interactions may be neglected in the slowing down process. Microscopically, energy losses due to excitations and ionizations are discrete processes. Macroscopically, one can assume that moving ions lose energy continuously. Theoretical treatments of inelastic collisions of charged particles with target atoms are separated into 'fast' and 'slow' collisions. The criterion is the velocity of the projectile relative to the mean orbital velocity of the atomic electrons in the shell or subshell of a given target atom.

Figure 7.9 shows the energy dependence of the stopping power for H^+ and He^+ in Al. An estimate of transition velocity between the slow and fast collision cases is the Bohr electron velocity, and this velocity is equivalent to that of 25 keV H^+, or 100 keV He^+. In practice, an incident ion beam with energies close to maximum electronic stopping can potentially give higher energy resolution.

The ability to distinguish between two types of target atoms that differ in their masses is determined by the ability of the experimental detectors to resolve small differences in the energy between backscattered particles. One of the most common detector types is a surface-barrier detector. This solid state nuclear particle detector operates by collection of the hole–electron pairs created by the incident particle in the depletion region. An incident ion will create holes and electrons on its penetration path: these holes and electrons will be separated by the bias applied between the front and back conductive layers.

The energy resolution in ion beam analysis is normally composed of two contributions: detector resolution and energy straggling. How we can define energy straggling? When an energetic ion moves through the material, it loses energy via many individual encounters. These discrete processes are subject to statistical fluctuations. As a result, identical energetic particles, with the same initial energy (velocity), do not have exactly the same energy after passing through a thickness Δx

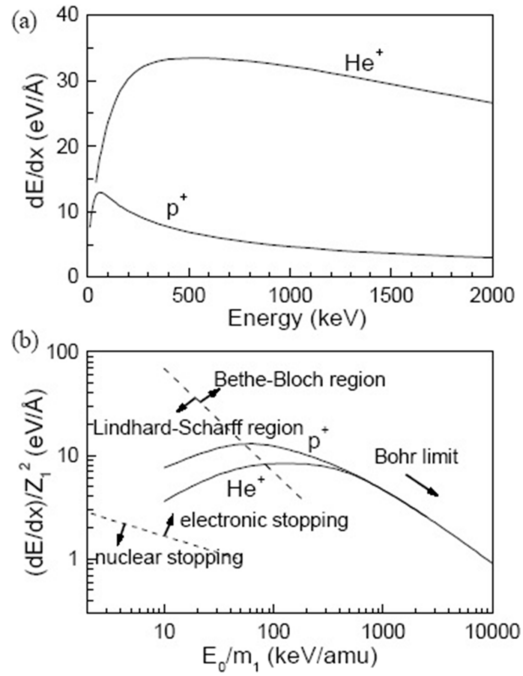

Figure 7.9. (a) Electronic stopping power (dE/dx) for protons and He^+ ions in Al versus energy, calculated by TRIM [4]. (b) The same data points are plotted on reduced axes which demonstrate the Bohr regime at high energy. The boundary between the Lindhard–Scharff and Bethe–Bloch regimes is shown. The regions in which the total stopping power is dominated by nuclear stopping and electronic stopping are shown.

of a homogeneous material. The energy loss ΔE will fluctuate due to straggling. Energy straggling gives a larger uncertainty, and therefore depth and thickness values will also be calculated with a limited precision.

The majority of elements can be determined in the backscattering spectra (RBS), however all light elements (H, He and Li) have low cross-sections, and an alternative method. Elastic recoil detection (ERD) is used for obtaining depth profiles of these light elements. While in RBS, a silicon barrier detector is typically placed at the scattering angles around 160–170 degrees (figure 7.10(a)); in ERD, the detector is mounted below angles of 90 degrees (figure 7.10(b)). When an incident beam, e.g. He^+, impinges on the sample surface, typically under the grazing angle, the surface atoms will be recoiled in a forward direction. Additionally, He ions will scatter in the forward direction as well. In order to block abundantly scattered helium ions from the detector, a thin (~10 μm) metal (Al) or Mylar foil is placed in front of the detector, permitting only the H ions through. The energy of the recoiled atoms, E_2, can be related to the incident energy E_o, by equation (7.7).

In ERD, depth profiles are determined by the energy loss of the incident He^+ in the forward direction and the energy loss of the recoil H^+ along the outward path for samples with different hydrogen profiles due to the diffusion or different sample treatments. The distribution of H in niobium and niobium oxide can be determined from spectra such as that shown in figure 7.11(a). Recent studies of the quality factor degradation mechanisms in superconducting RF niobium cavities at high surface magnetic fields revealed that RF performance may depend on the total hydrogen content in the 40 nm thick near-surface layer. Hydrogen distribution in niobium and its near-surface content variations after different chemical surface treatments has been addressed in this example [9]. Another notable feature is the amount of hydrogen coming from hydrocarbon particles present at the surface of any samples passing through ambient conditions, which is another source of uncertainties during quantification.

The stopping foil does introduce energy straggling, which combined with the energy resolution of the detector results in an energy resolution at the sample surface of about 20–40 keV. The best sensitivity for hydrogen using an ERD analysis was shown by Nagai *et al* [10] to be 10^{12} hydrogen atoms/cm^2 or approximately 1 weight ppm. But the typical value for the sensitivity of the most detectable elements in ERD is 0.1 atomic percent.

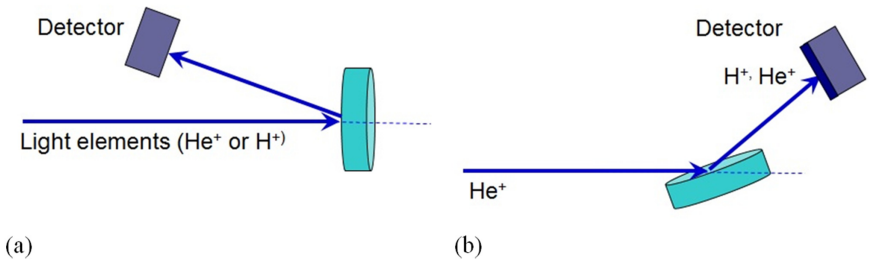

Figure 7.10. Experimental geometry for (a) Rutherford backscattering spectroscopy and (b) elastic recoil detection.

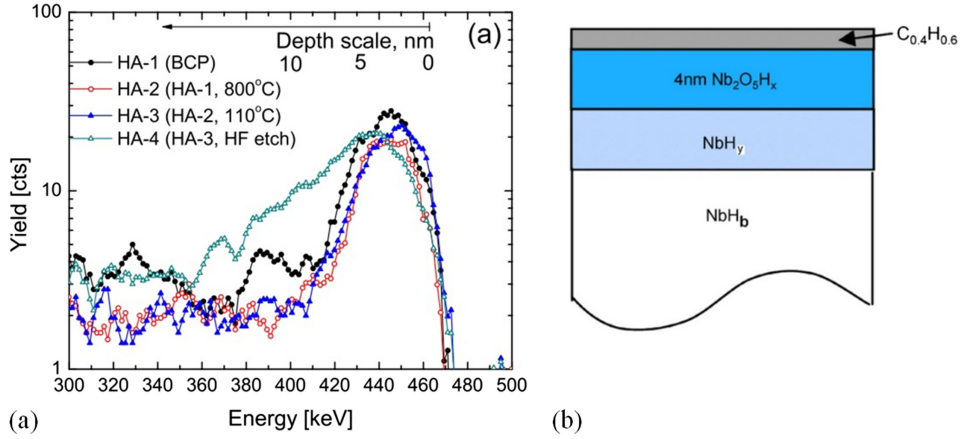

Figure 7.11. (a) Experimental ERD spectra for 2.9 MeV He^+ and (b) surface structure of Nb assumed from ERD data fitting. Reproduced from [9] with permission of IOP Publishing.

7.5 Secondary ion mass spectrometry (SIMS)

Surface layers are eroded by the sputtering process, as illustrated in figure 7.1, and the sputtering species provide a direct measure of the composition of the layer that has been removed. Secondary ion mass spectrometry (SIMS) is the mass spectrometry of ionized particles emitted from a solid surface when it is bombarded by primary energetic particles. The primary beam can be ions, or neutrals, or a laser. The emitted particles are electrons, neutral atoms or molecules, atomic and molecular ions, both positive and negative. The ratio of ionized to neutral species from the same sample can vary by an order of magnitude depending on the condition of the surface (matrix effect). In SIMS, mass spectrometers are often used as detectors. In one mode of operation, the sputter ion beam is rastered across the surface where it erodes a crater in the surface. To ensure that ions from the crater walls are not detected, the detection system is gated for ions from the central portion of the crater. The spectra of both positive and negative secondary ions are complex, exhibiting not only single and multiple charged atomic ions but all ionized clusters. As shown in figure 7.12, the mass spectrum from a O_2^+ bombarded iron oxide shows not only single ionized atoms and compound clusters but also double and triple ionized clusters. Significantly, the yield of one of the predominant Fe^+, FeO^+ secondary ions is strongly dependent on residual oxygen pressure during analysis.

The sputtering yield for a particular sample is important for SIMS analysis. Moreover, secondary ion yield strongly depends on the chemical environment (matrix effect). For instance, the yield of Si^+ from SiO_2 will be different by orders of magnitude from Si^+ in Si. The intensity of secondary ions can be expressed by the following:

$$I_{A+}^T = j_p \times A \times Y_{A+}^T \times f \times C_{A+}^T \tag{7.16}$$

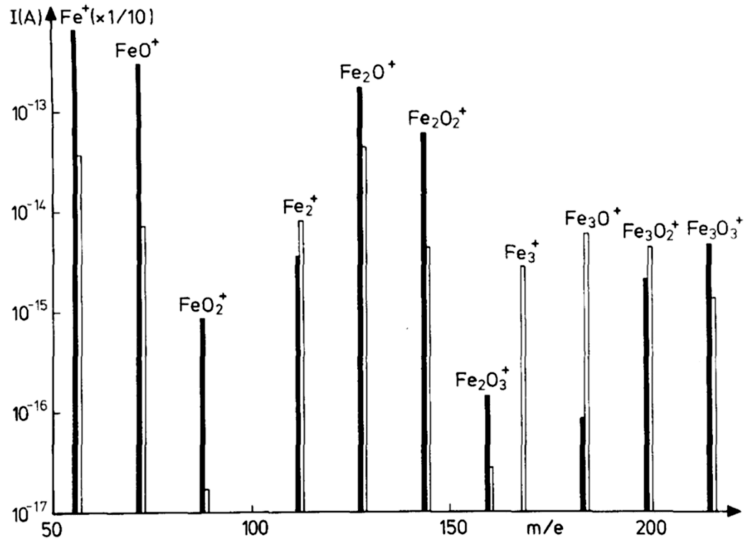

Figure 7.12. Positive secondary ion cluster spectrum of iron resulting from 6 keV O_2^+ bombardment with a spot of 300 mm diameter rastered across ~1 mm^2. Open bars are in a vacuum of 2×10^{-7} Torr, solid bars are in partial oxygen pressure 3×10^{-5} Torr. Reproduced from [11] with permission of Springer.

where I is the measured ion current of A^+ in the matrix T, j_p is the primary ion current density, A is the area of analysis, Y is the secondary ion yield in the matrix T, f is the instrumental transmission factor for A, and C is the atomic concentration of A in the matrix T. In turn, secondary ion yield is dependent on the ionization probability, which is another parameter strongly influenced by the matrix.

A good example of SIMS depth profiling is the measurement of ion implanted impurity in semiconductors (figure 7.13) [12]. The maximum dopant concentration is below 10^{-3} and the presence of As has an insignificant effect on the ionization probability. Another strong feature of SIMS is the ability to analyze hydrogen over a wide range of concentrations. In these cases, surface contamination by water can change the dynamic range.

Another variant of SIMS uses a time-of-flight mass spectrometer. Owing to its sensitivity, TOF SIMS is especially suited to study delicate biological or organic materials. For example, TOF-SIMS has been used to study the formation of thiol-based self-assembled monolayers (SAM), such as dodecanethiol on Au films, with an example of TOF-SIMS spectrum presented in figure 7.14 [13]. TOF-SIMS easily confirmed self-assembled monolayer formation, its electrochemical removal, and the subsequent formation of another SAM in its place.

7.6 Low- and medium-energy ion scattering

Finally, two lower in incident energy RBS-related techniques have evolved in the past several decades: low- and medium-energy scattering. Medium-energy ion

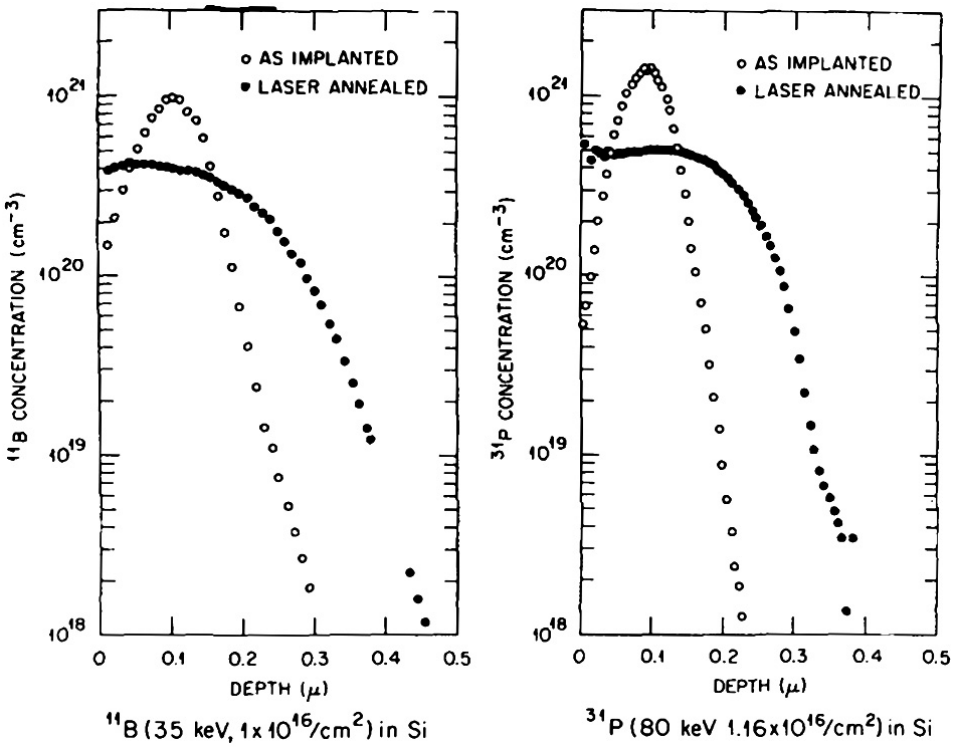

Figure 7.13. SIMS concentration profiles of (a) B and (b) P implanted in Si and distributed by pulsed laser annealing of the surface Si layer. Reprinted from [12], with the permission of AIP Publishing.

scattering (MEIS) is another fairly new and still not very common variant of RBS. In MEIS, light ions (usually H^+ or He^+) with an energy of 40–400 keV are incident along a major crystallographic direction in the solid. Energy- and angle-resolved detection of backscattered ions provides structural and compositional information. Among the high-resolution detectors introduced in the past two decades, two detectors—the electrostatic energy analyzer (ESA), and time-of-flight (TOF)—have been most commonly used in MEIS systems.

Figure 7.15(a) shows a window from the MEIS data acquisition program containing raw scattering data from an ESA detector for a 98 keV proton beam normally incident on the surface of a Fe-9%W(100) alloy. The scale perpendicular to the page represents the detected yield of scattered ions (dark areas have high counts). Two types of spectra are gathered from this raw data: energy spectra, figure 7.15(b), and angular spectra, figure 7.15(c) [14].

Quite generally, methods exist to utilize either the energy or angular spectra from the raw data to access either structural or compositional information. Energy spectra are formed by summing data in a narrow angular range as a function of energy. The area of the As peak directly gives the surface coverage of this element with good accuracy and sensitivity. The detailed shape of these signals (especially for

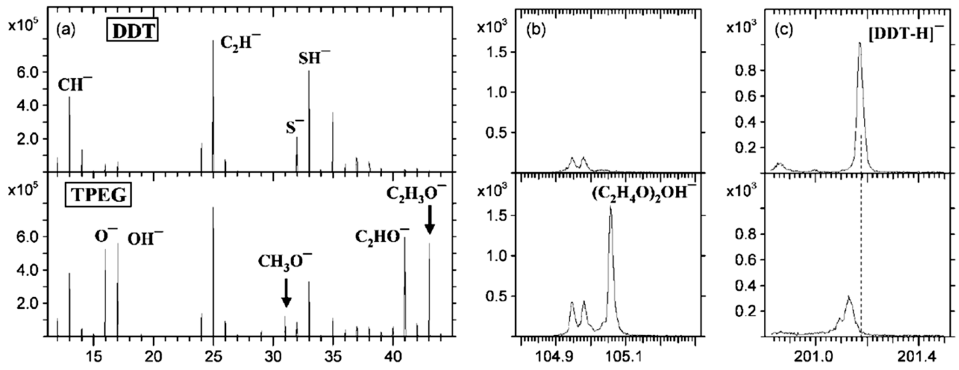

Figure 7.14. Negative secondary ion mass spectra for dodecanethiol self-assembled monolayers on Au. Reprinted from [13] with permission.

thin films) can be used to get depth profile information, and in some cases information about the structure can be obtained. Angular spectra are obtained by integrating the surface peak area of a given element as a function of the scattering angle. This is shown for Fe and As above. Basic geometrical considerations and comparison to ion scattering simulations provide detailed structural information from the angular spectra, such as interlayer separations and vibrational amplitudes.

Low-energy ion scattering uses keV ions that scatter predominantly from the surface layer and are considered extremely sensitive for the first monolayer analysis. Quantitative analysis in this regime is less straightforward since there are larger uncertainties in the absolute cross-sections and a lack of accurate neutralization of the surface scattered particles. However, there are many recent examples where LEIS was used to investigate dynamic processes such as thin film growth, closure and formation of pinholes in thin films [15], catalysis poisoning and activation [16], formation of nanoparticles [17]. For instance, surface termination and subsurface restructuring of perovskite-based solid oxide electrode materials was probed by LEIS in the work of Druce *et al* [18].

Perovskite-based (ABO_3) ceramics have many applications, including ferroelectrics, multiferroics and electro-catalysis in high temperature electrochemical devices. One subgroup, the $A^{3+}B^{3+}O_3$ (3,3) perovskites, are extensively used as electrode materials in solid oxide fuel cells and electrolyzers. Several different perovskite and perovskite-related structures are shown in figure 7.16. Prior to LEIS analysis, all samples were exposed to atomic oxygen to remove any hydrocarbon contamination from exposure to atmosphere.

LEIS spectra of different perovskite samples are shown in figure 7.17. The top surface layer of all the materials after a typical high-temperature treatment in oxidant ambient are dominated by A-site cation. Furthermore, LEIS results show the dynamic nature of the outermost atomic layers of electroceramic materials. Significant surface modifications can occur after thermal treatments typical in the processing and operation of these materials [18].

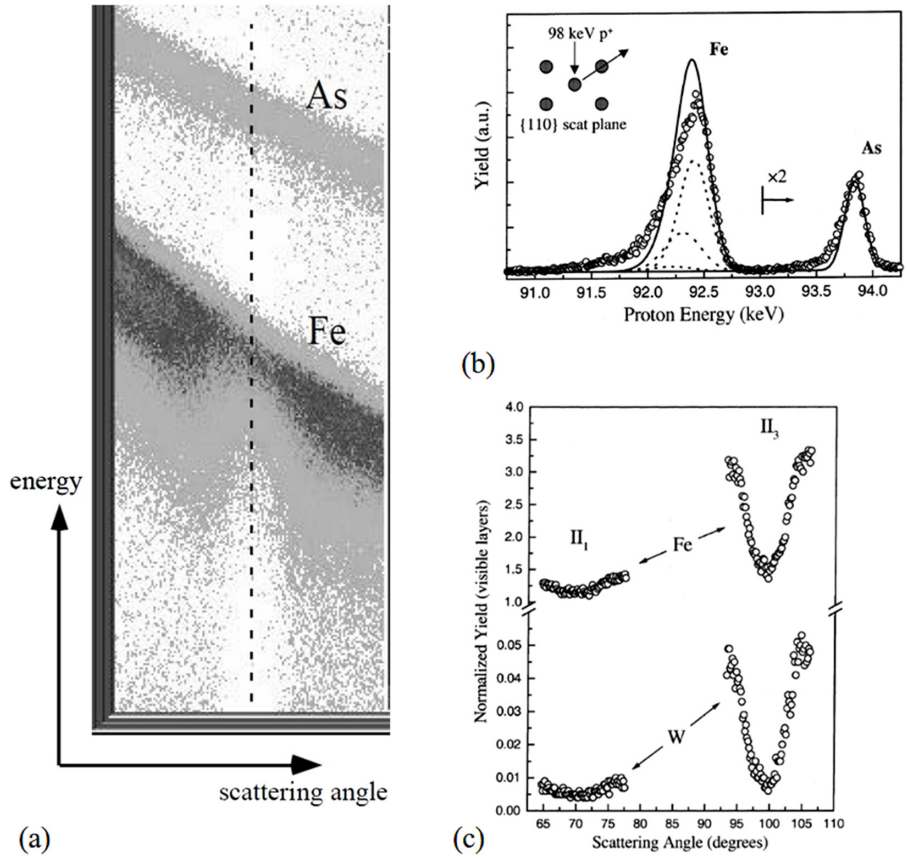

Figure 7.15. (a) Window from the data acquisition program showing raw proton scattering data from the Fe-9%W (100) surface. The grayscale indicates the detected counts in each energy (vertical) and angle (horizontal) channel. (b) Energy spectrum (yield versus energy at some scattering angle) from the data in (a). (c) Angular spectra from Fe and As in different azimuth scattering geometries (II_1 and II_3). Reprinted from [14], Copyright 2001 with permission from Elsevier.

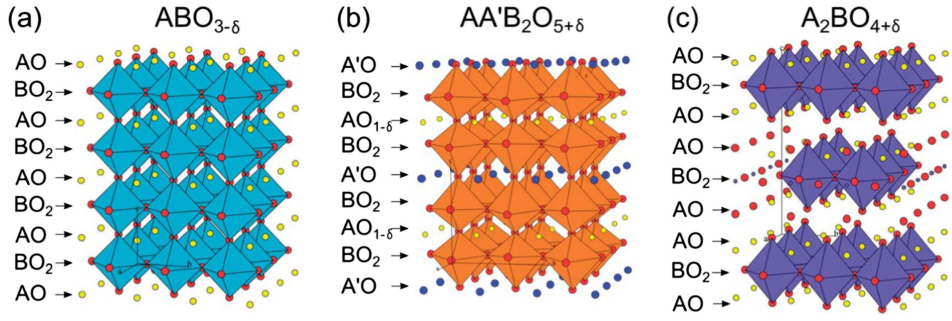

Figure 7.16. Structures of the perovskite and perovskite-related oxides. (a) ABO_{3-d}, (b) ordered double perovskite, $AA'B_2O_5$, and (c) Ruddlesden–Popper structure $A_2BO_{4+\delta}$. Reproduced from [18] with permission of The Royal Society of Chemistry.

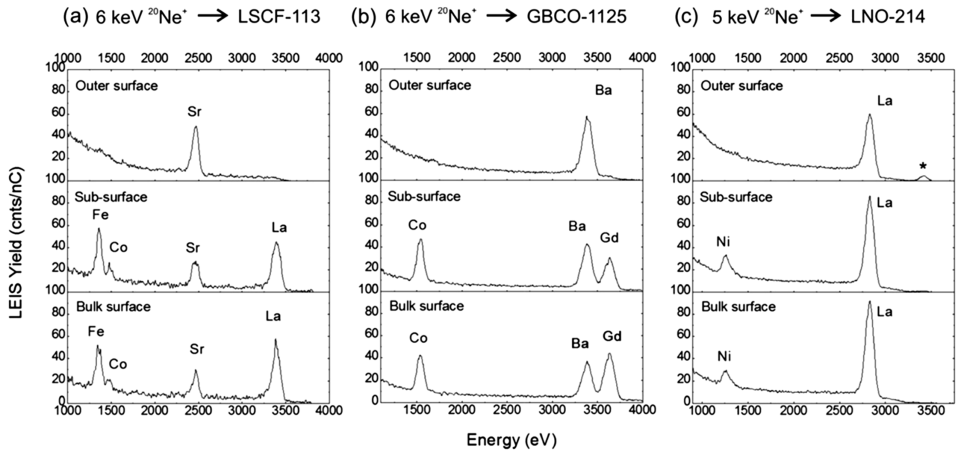

Figure 7.17. LEIS spectra of (a) ABO_{3-d}, (b) ordered double perovskite, $AA'B_2O_5$, and (c) Ruddlesden–Popper with $A_2BO_{4+\delta}$ structures. Reproduced from [18] with permission of The Royal Society of Chemistry.

7.7 Exercises

1. If you use alpha particles ($M_1 = 4$ amu) with incident energy $E_o = 2$ MeV, the detector is at $\Theta = 180°$, and your target is a ~100 Å thick gold film on top of silicon substrate, find your energy positions of Si and Au elements in a Rutherford backscattering spectrum. Draw the RBS spectrum schematically but mark the energy positions for all observed features.
2. Silicon nanocrystals (Si-ncs) embedded in SiO_2 exhibit strong luminescence at room temperature and are of interest in the drive to produce silicon photonic devices that are compatible with silicon processing techniques. Formation of Si-ncs can be done using ion implantation of excess silicon into SiO_2 film followed by high temperature annealing (nucleation and growth via Ostwald ripening).
   (a) Your sample is composed of 100 nm SiO_2 film on top of a Si(001) substrate. Use SRIM to find the incident energy of Si ions to place excess Si atoms in the middle of the SiO_2 layer (assume that the implantation angle is 10 degrees).
   (b) To achieve excess silicon in a SiO_2 layer, one has to use an implantation dose as high as 1×10^{17} Si atoms/cm^2. As a result of Si-ncs formation, the SiO_2 layer expands or 'swells'; because of this effect the thickness of SiO_2 layer becomes higher. Calculate this increase in SiO_2 layer thickness, assuming a simplified model when 100% of implanted Si forms Si-ncs that are cubic in shape with the dimensions $d = 3 \times$ a lattice constant of Si (a_{Si}). As a reminder, Si has a diamond lattice structure with the lattice constant $a = 5.43$ Å.
3. From RBS measurements you found the atomic density of Fe atoms in the Fe film on carbon substrate as 3×10^{16} atoms/cm^2. Calculate the physical

thickness of the Fe film, in nm, assuming the density of Fe in the film is 90% of the bulk density (7.087 g cm^{-3}).

References

[1] Feldman L C and Mayer J W 1986 *Fundamentals of Surface and Thin Film Analysis* (Englewood Cliffs, NJ: Prentice Hall)

[2] Wang Y and Nastasi Y M 2010 *Handbook of Modern Ion Beam Materials Analysis* 2nd edn (Cambridge: Cambridge University Press)

[3] Lindhard J, Scharff M and Schiott H E 1963 *Mat. Fys. Medd. Dan. Vid. Selsk* **33** 14

[4] Ziegler J F and Biersack J P 2008 *SRIM - The Stopping and Range of Ions in Matter* **Ver.2008**

[5] Andersen H H and Bay H L 1981 *Sputtering by Particle Bombardment* ed R Behrisch (New York: Springer)

[6] Liau Z L and Mayer J W 1980 *Ion Implantation* ed J K Hirvonen (New York: Academic) vol 18

[7] Doerner R P, Whyte D G and Goebel D M 2003 *J. Appl. Phys.* **93** 5816–23

[8] Eckstein W and Preuss R 2003 *J. Nucl. Mater.* **320** 209–13

[9] Romanenko A and Goncharova L V 2011 *Supercond. Sci. Technol.* **24** 105017

[10] Nagai H, Hayashi S, Aratani M, Nozaki T, Yanokura M, Kohno I, Kuboi O and Yatsurugi Y 1987 *Nucl. Instr. Methods Phys. Res.* B **28** 59–66

[11] Morgan A E and Werner H W 1976 *Appl. Phys.* **11** 193–5

[12] White C W, Christie W H, Appleton B R, Wilson S R, Pronko P P and Magee C W 1978 *Appl. Phys. Lett.* **33** 662–4

[13] Tencer M, Nie H Y and Berini P 2011 *Surf. Interface Anal.* **43** 993–7

[14] Busch B W, Schulte W H, Gustafsson T and Uebing C 2001 *Nucl. Instr. Methods Phys. Res.* B **183** 88–96

[15] Delabie A *et al* 2005 *J. Appl. Phys.* **97** 064104

[16] Tanabe T 2009 *Appl. Catal.* A **370** 108–13

[17] Kauling A, Ebeling G, Morais J, Padua A, Grehl T, Brongersma H H and Dupont J 2013 *Langmuir* **29** 14301–6

[18] Druce J *et al* 2014 *Energy Environ. Sci.* **7** 3593–9